The effect of segmentation depth in a helical fin tube bundle on the anisotropic turbulence state

M. A. García-Andrade[a], E. Martínez-Espinosa[a], M. Salinas-Vázquez[a,*], J. Ramírez-Cruz[b], W. Vicente[a], and J. Rosas-Flores[b]

[a]*Instituto de Ingeniería, Universidad Nacional Autónoma de México,*
04510, Mexico Ciudad de México.
[b]*Facultad de Ingeniería, Universidad Nacional Autónoma de México,*
04510, Mexico Ciudad de México.
* msalinasv@iingen.unam.mx

The large eddy simulation approach was used to perform a numerical simulation of a flow around a helical segmented-fin tube bundle. This work focuses on the study of turbulence and the effect of segment depth on it. The simulation was conducted in an area away from the boundaries of the tube bundle, where the flow is fully-developed, and the use of periodic boundary conditions is possible. The computer-aided design of the helical segmented-fin tube geometry is incorporated into the computational grid from the immersed boundary technique. The Reynolds stress tensor was used to analyze the anisotropic state of turbulence. This flow is characterized by an anisotropic state generated by a flow with a preferential direction. A transfer of momentum in the inter-segment space and contiguous zones was observed. This inter-segment flow generates a less anisotropic state of turbulence. This study aimed to understand a possible transformation of heat transfer with marginal geometrical changes and pressure drop increases.

1. Introduction

Helical segmented-fin or serrated-fin tubes are widely used in heat exchangers because the heat transfer surface decreases, and consequently, the weight of the thermal equipment is reduced. The heat transfer performance is not sacrificed because the geometry of finned tubes promotes turbulence, although the pressure drop also increases. In the open literature, experiments and numerical simulations have studied the thermal-hydraulic behavior of helical segmented-fin (serrated-fin) tubes. Most experiments present global studies of heat transfer and pressure drop on finned tube banks [1-5]. Some works compare the thermal performance of different serrated-fin geometries, as developed by Zhou *et al*. [1]. Other studies analyze the effect of segmented-fin (serrated-fin) characteristics, such as fin pitch, fin height, fin density, and segmented fin height on heat transfer and pressure drop. For instance, heat transfer and pressure drop increase as fin height and fin density increase, as reported by Naess [2] and Ma *et al*. [3]. In contrast, the fin pitch has a reverse behavior because heat transfer and pressure drop decrease, as found in Naess [2] and Kiatpachai [4]. Keawkamrop *et al*. [5] found that segmented fin height significantly affects the Nusselt number. Some experiments report detailed information as visualizations [6, 7] and velocity measurements [8]. For example, Pis'mennyi [6, 7] identified experimentally intense vortical structures in the front of the fins, which increased the transfer of momentum and energy. Papa [8] measured the velocity field and turbulence parameters in half of a finned tube.

On the other hand, numerical simulations present detailed information on the heat transfer performance of a single-finned tube [9–13] or a small-finned tube bundle [1, 14–22]. Most numerical simulations focus on representing the flow around the finned tube and its connection to heat transfer [1,9-11,14,15,17,18,20,21]. For example, Martínez-Espinosa *et al*. [18] found intense temperature gradients near the vertex of segmented fins where heat transfer is intense. Other investigations included parametric studies of fin characteristics (segmented fin height, fin pitch, fin height, or fin thickness) on heat transfer [12,13,16,19]. Anoop *et al*. [12] found that segmented fin height has the same thermal performance as plain fins, with less heat transfer area. Finally, few works have studied the turbulent structures in helical segmented-fin tubes and their relation to energy transport. Kumar *et al*. [19] found vortices generated by fins and horseshoe vortices along the tube surface that enhanced the heat transfer. These vortices were identified through vector maps and streamlines in a RANS) simulation (Reynold Average Navier Stokes). Salinas-Vázquez *et al*. [22] found relevant momentum transfer in the inter-segment space, which increased the turbulence and the formation of vortices between the fins at high spaces between the segments.

State-of-the-art research reveals that few works have studied turbulent structures in helical segmented-fin tubes [19, 22]. Studies of heat transfer performance reveal that heat transfer is intense in the vertex of segmented fins [5, 18] and influenced by the presence of vortices in these zones [6]. Few studies have been conducted on turbulence structures and their connection to heat transfer and pressure drop in he-

lical segmented-fin tubes. Therefore, this study continues the turbulence study developed by Salinas-Vázquez *et al.* [22] while considering studies on the vertex of segmented fins conducted by Martinez-Espinosa *et al.* [18] and Keawkamrop *et al.* [5]. The primary objective is to propose a way to increase the thermal performance of helical segmented fins without an increase in pressure drop and heat transfer surface. Then, a numerical study of the anisotropic state of the turbulence is developed at different segmented fin heights. Simulations were conducted using the large eddy simulation (LES) approach and numerical tools, such as periodic boundary conditions and the immersed boundary technique. Four cases were simulated at different segmented fin heights to understand the effect of the depth of the fin segmentation on thermal-hydraulic performance.

2. Governing equations

The compressible Navier-Stokes equations in a Cartesian frame of reference can be written as follows [23]:

$$\frac{\partial \boldsymbol{U}}{\partial t} + \frac{\partial F_i}{\partial x_i} = \boldsymbol{S_F}, \quad (1)$$

where $\boldsymbol{U}$ is the vector of conservative variables, defined as:

$$\boldsymbol{U} = (\rho, \rho u_1, \rho u_2, \rho u_3, \rho e)^T, \quad (2)$$

where u_i represents the velocity component in the $i-$direction, and ρ is the density. In the results section, both the velocity and space direction vectors were changed from (u_1, u_2, u_3) to (u, v, w) and (x_1, x_2, x_3) to (x, y, z), respectively. The total energy, which is the sum of internal and kinetic energies, is defined for an ideal gas as follows:

$$\rho e = \rho c_v T + \frac{1}{2}\rho\left(u_1^2 + u_2^2 + u_3^2\right), \quad (3)$$

$\boldsymbol{F_i}$ is the fluxes in the three spatial directions.

$$\boldsymbol{F_i} = \begin{pmatrix} \rho u_i \\ \rho u_i u_1 + \frac{1}{\gamma M^2}p\delta_{i1} - \frac{\mu}{Re}S_{i1} \\ \rho u_i u_2 + \frac{1}{\gamma M^2}p\delta_{i2} - \frac{\mu}{Re}S_{i2} \\ \rho u_i u_3 + \frac{1}{\gamma M^2}p\delta_{i3} - \frac{\mu}{Re}S_{i3} \\ (\rho e + P)u_i + \frac{\gamma M^2}{Re}\mu S_{ij}u_i - \frac{\gamma}{\gamma-1}\frac{k}{PrRe}\frac{\partial T}{\partial x_i} \end{pmatrix}, \quad (4)$$

where k is thermal conductivity, δ_{ij} is the Kronecker delta, and S_{ij} is the deformation tensor, defined as:

$$S_{ij} = \frac{1}{2}\left(\frac{\partial u_i}{\partial x_j} + \frac{\partial u_j}{\partial x_i} - \frac{2}{3}\left(\nabla \cdot u\right)\delta_{ij}\right). \quad (5)$$

The vector S_F, corresponding to the source terms, is a function of time only and is necessary to counteract the friction losses in the principal direction. Force must be introduced to represent a fully-developed flow economically (Fig. 1a) by imposing a constant mass flux in the periodic main flow

direction. This forcing term, $f_s(t)$, is equivalent to the imposition of a mean streamwise pressure gradient (see the appendix in Salinas *et al.* [22]). The forcing appears in the energy equation multiplied by the mean bulk velocity Eq. (7).

$$\boldsymbol{S_F} = (0, f_s(t), 0, 0, U_b f_s(t))^T. \quad (6)$$

3. Numerical solution

3.1. Numerical scheme

Equations (1) to (4) in the generalized coordinates were solved using the fully explicit McCormack scheme [24], second order in time, and fourth order in space.

3.2. Initial and boundary condtions

The thermodynamic variables, temperature, and pressure (or density) were initialized by a constant value and equal to their reference values of T_{ref} and P_{ref} (atmospheric conditions). The tube temperature is constant through the simulation and equal to $T_{tube} = 1.4T_{ref}$. The streamwise velocity ($x-$direction) was equal to its reference value of $U_0 = U_b$, which was the bulk flow velocity in the domain, defined as:

$$U_b = \frac{(\rho u)_b(t)}{(\rho)_b(t)}. \quad (7)$$

The mean bulk value of a variable is given by:

$$(\varnothing)_b(t) = \frac{1}{\mathbf{V}_{\text{Free\_Total}}} \iiint \varnothing(\vec{x}, t)\,\delta_b(\vec{x})\,dx\,dy\,dz, \quad (8)$$

where $\delta_b(\vec{x}) = 1$ Free volume, $\delta_b(\vec{x}) = 0$ blocked volume, solid body, $V_{\text{Free_Total}} = $ total volume of comp. domain.

Two spanwise velocity components ($y-z$ direction) were considered null ($V_0 = 0$ and $W_0 = 0$). Periodic boundary conditions were applied in the $x-$ and $y-$directions. Physically, this implied that the lateral walls did not influence any of the two directions. This condition consists of cloning the computation domain in the periodic directions, see Fig. 1a). This boundary condition allows the simulation of an infinity of tubes at the fully developed zone of the tube bundle (after four to five rows of the inlet and far from the lateral walls [25]) while saving computer resources. A forcing term (Eq. (6)) must be imposed to prevent the flow stop and the creation of the pressure drop, a non-periodic condition (see Appendix in Ref. [22]). Slip walls [26] were imposed in the z-direction. The boundary condition is based on the method called Navier Stokes characteristic boundary conditions. The hyperbolic terms of equations are modified at the boundary by characteristic analysis in the form of waves normal to the boundary. For slip wall, an invisid conditions is imposed at the wall: $u_{\perp wall} = 0$. The tangential shear viscous stresses parallel to the wall and the heat transfer normal to the wall are null (viscous conditions). The momentum normal to the
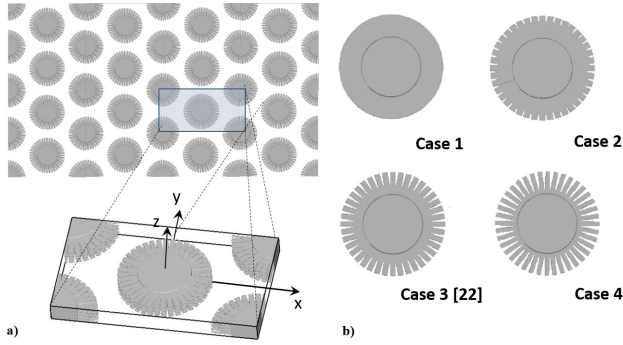
FIGURE 1. Periodic boundary conditions and fin configuration a) numerical domain and physical representation of periodic boundary conditions and b) fin characteristics for the four studied cases.
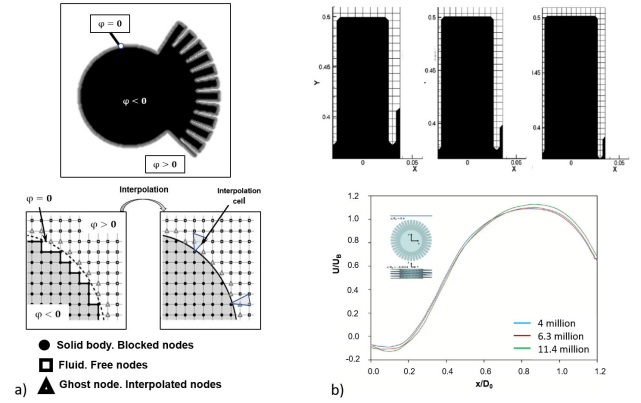

FIGURE 2. Immersed boundary conditions and grid independence. a) Immersed boundary conditions based in the use of a level set function φ. Interpolation of the solid body variable values avoids the stepping behavior. b) Fin representation in three different grid resolutions. Mean streamwise velocity comparison for three different grid resolutions.

wall and energy are not computed on the boundary. The rest of the variables are obtained from the conservation equations in function of the normal wave amplitudes associated with the characteristic velocities of the system.

3.3. Turbulence model

The turbulent effects were simulated with a LES model. According to Metais and Lesieur [27, 28], small scales should be filtered, and their effects included in the present model through the classic eddy-viscosity assumption, (ν_t). The subgrid-scale model used in this work is the selective structure-function model proposed by [29]. The local eddy viscosity, $\nu_t(x,t)$, is then given by:

$$\nu_t(x,t) = C_{ssf}\Delta(F^2(x,t))^{1/2}, \qquad (9)$$

where C_{ssf} is expressed as a function of the Kolmogorov constant C_k, $C_{ssf} = 0.104$. Local filter size, Δ, is taken equal to $(\Delta x \Delta y \Delta z)^{1/3}$, where Δx, Δy, and Δz are the local grid sizes in the three spatial directions. $F^2(x,t)$, the second-order velocity structure function constructed with the instantaneous filtered field. $F^2(x,t)$ is calculated at a given point with a local statistical average of square (Favre-filtered) velocity differences between the given point and the six closest points surrounding the computational grid.

3.4. Immersed boundary conditions

Immersed boundaries allow solid bodies with complex geometries to be introduced into the flow. The complex solid body geometry of the fins was generated using computer-aided design software in STL format (Standard Triangle Language) and transferred to the computational domain (own numerical tool).

To identify the solid, we used a level set function, $\varphi(x)$, which took the value of $-\alpha$ inside the solid and $+\alpha$ outside the solid. α is proportional to the maximum grid size in the computational domain [22, 30, 31]. Ghost nodes were identified as those nodes that are close to the solid body without being part of it(see Fig. 2a).

After a reinitialization process of the level set function [30,31] to keep $\varphi(x)$ as a signed distance function. The solid surface was obtained with good precision at the zero-level of this function ($\varphi(x) = 0$). The solid body was created by imposing harsh conditions, such as null velocities and a constant temperature, at the blocked nodes ($\varphi(x) < 0$, see Fig. 2). The velocity at the ghost points was interpolated (linear 2d and 3d interpolations) from the values of their nearest neighbor nodes. This procedure avoided a stepping behavior of the velocity field close to the walls; the complete procedure can be seen in [32]. The pressure was extrapolated from the fluid to the solid [33], which allowed for a null pressure gradient at any wall surface, $\partial p/\partial n|_{wall} = 0$. The extrapolation was obtained from the following advection equation:

$$\frac{\partial p}{\partial \tau} + n \cdot \nabla p = 0, \qquad (10)$$

where n is the normal to the wall unit at every grid point, defined from the level set function, φ as:

$$n = \frac{\nabla \varphi}{|\nabla \varphi|}, \qquad (11)$$

where τ is not the physical time, but a function of the grid $\tau \propto \min(\Delta x \Delta y \Delta z)$. Five time steps were required to populate the needed nodes. Advection equation Eq. (10) was solved using a third-order total variation diminishing (TVD) Runge-Kutta scheme for time discretization and a fifth-order weighted essentially non-oscillatory (WENO) scheme for space discretization [34]. The extrapolation procedure was done for every time step of physical time, t.

4. Validation

The validation was conducted in two stages. In the first, the numerical and experimental results obtained by Simonin and Barcouda [25] were compared in a smooth tube bundle [32]. In the second stage [22], the mean streamwise velocity was compared with the experimental results [8].
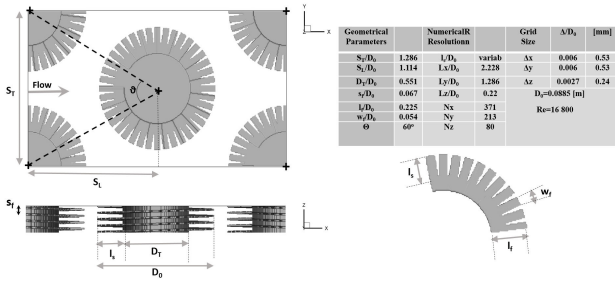
Geometrical Parameters		Numerical Resolution		Grid Size		Δ/D₀	[mm]
S_T/D_0	1.286	L/D_0	variab	Δx	0.006	0.53	
S_L/D_0	1.114	Lx/D_0	2.228	Δy	0.006	0.53	
D_T/D_0	0.551	Ly/D_0	1.286	Δz	0.0027	0.24	
s_f/D_0	0.067	Lz/D_0	0.22	D_0=0.0885 [m]			
l_f/D_0	0.225	Nx	371	Re=16 800			
w_f/D_0	0.054	Ny	213				
Θ	60°	Nz	80				

FIGURE 3. Geometrical characteristics and resolution of the studied numerical domain.

5. Simulation characteristics

The computational domain was the same as in a previous study [22]. The reduced domain comprised a complete tube at the center and four quarters in the corners (see Fig. 2). In this work, only the hydrodynamics of the fluid were studied. The Reynolds number $(Re = (U_b D_0 \rho_{ref})/(\mu(T_{ref})))$ used in this study was 16890 (equal to that used in Martinez *et al.* [18] and Salinas-Vázquez *et al.* [22]. The dimensionless computational domain lengths are $(D_0 = 0.0508$ m): $2.228 D_0 \times 1.286 D_0 \times 0.22 D_0$ for the $x-$, $y-$, and $z-$directions, respectively. Due to the complexity of the tubes, the grid was uniform in all three directions. The grid resolution is $371 \times 213 \times 80$ computational nodes for the $x-$, $y-$ and $z-$directions.

This resolution was obtained after studying the independence between the grid resolution and the results [35]. For this flow, the main difficulty was correctly capturing the geometry of the fins. In Fig. 2b), we show the fin resolution for three different cases (4, 6.3, and 11.4 million computational nodes). We found that for resolutions 50% lower than the one used here, significant changes $(2-3\%)$ were not observed in the statistical results. Figure 2b) shows the comparison of the mean streamwise velocity in a given position. The same behavior was observed in mean and turbulence quantities.

In engineering, the best solutions are the simplest. For this reason, the present work intends to complement previous works [22] on the subject by changing the fin segmentation depth, l_s. Four different configurations [Fig. 1b)] were studied: $l_s/l_f = 0.0$ (smooth fin), 0.25, 0.5 (base case [22]), and 0.75, where l_f is the total fin length and l_s is the segmentation depth [see Figs. 1b) and 2b)]. The flow characteristics, computational domain length, and resolution were the same for all cases (Fig. 3).

5.1. Statistical variables

We define the mean quantities as the average of the variable across time. For any given instantaneous quantity $f(\vec{x}, t)$, the mean was written as $F(\vec{x})$. No spatial averaging in the periodic directions was possible for this configuration. The instantaneous fluctuation $f'(\vec{x}, t)$ from the mean satisfies $f'(\vec{x}, t) = f(\vec{x}, t) - F(\vec{x})$. The term "rms" indicates that the fluctuating values are defined, as in the following:

$$u'_{rms} = \langle u'_i u'_i \rangle^{1/2}, \tag{12}$$

where $\langle u'_i u'_i \rangle$ are the normal Reynolds stresses. The Reynolds stress anisotropy tensor b_{ij}, normalized with the turbulence kinetic energy $(k = (1/2) \langle u'_k u'_k \rangle)$, is defined to quantify deviation from an isotropic stress field:

$$b_{ij} = \frac{\langle u'_i u'_i \rangle}{\langle u'_k u'_k \rangle} - \frac{1}{3}\delta_{ij}. \tag{13}$$

The second and third invariants of the tensor are defined as [36]:

$$II = b_{ij} b_{ji}/2,$$
$$III = b_{ij} b_{jk} b_{ki}/3. \tag{14}$$

Based on the previous invariants, the η and ξ variables are defined as [36–38]:

$$\begin{aligned} \eta^2 &= II/3 \\ \xi^3 &= III/2. \end{aligned} \tag{15}$$

The anisotropic state of turbulence can be described by a characteristic spheroid whose radii correspond to the eigenvalues [37]. The anisotropic state of turbulence parameter $[F]$ scales the degree of anisotropy from zero (one- or two-component turbulence, anisotropy) to one (isotropic turbulence), and it is defined as [36–38]:

$$[F] = 1 - 27\eta^2 + 52\xi^3. \tag{16}$$

6. Results

6.1. Mean streamwise velocity

Figure 4 shows the mean streamwise velocity in a z-plan. The darker blue zones (negative velocity values) show recirculation zones. As seen in previous works [22], the mean velocity field shows a pair of symmetrical recirculations behind the
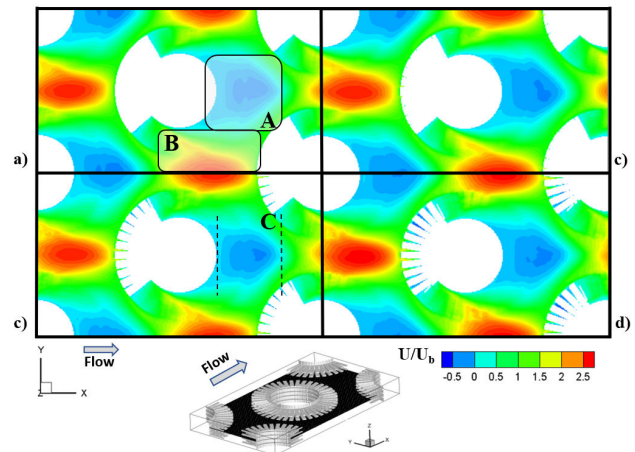

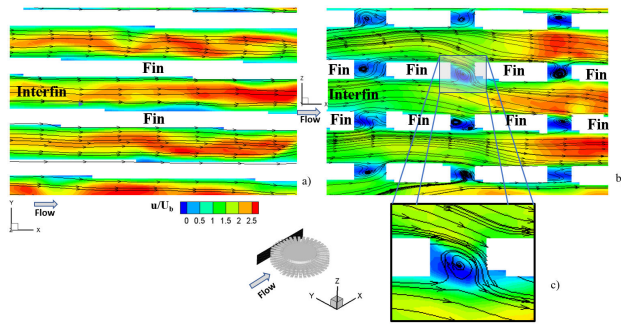FIGURE 4. Mean streamwise velocity in a z-plane, $z/D_0 = 0.11$ for a) Case 1, b) Case 2, c) Case 3, and d) Case 4.

FIGURE 5. Instantaneous streamwise velocity contours and trajectory lines in the y-plane, $y/D_0 = 0.44$, a) Case 1, b) Case 4, and c) flow from one interfin zone to another (Zoom Case 4).

tubes (dark blue zones, A-square) and high-velocity bands away from the tubes (red zones, B-square). However, several antisymmetric recirculations were observed in instantaneous fields [22]. Recirculation size (C-lines) and the minimal and maximal mean streamwise velocity values were similar for all cases studied. A comparable situation was observed for the other components. Small changes in velocity fields bring with them minimal changes in pressure drop. A great advantage in heat exchanger design is the marginal increase of $< 2\%$ in the pressure drop observed between Cases 1 and 4.

6.2. Interfin zone interactions

The main change in the flow for the different cases studied was found in the interfin zones. The interaction between these zones is shown from instantaneous velocity fields. Figure 5 shows the trajectory lines in the y-plane. The flow goes from one zone to another through the spaces made by the fin segmentation (Fig. 5c). The instantaneous and mean magnitude of the normal velocity component increases in this zone.

6.3. Turbulence intensities

Figure 6 shows the turbulence intensities (rms-values) and the turbulence kinetic energy ($k = (1/2) < u'_k u'_k >$), in a z-plane. Contours show a decrease from Case 1 to 4 in the u'_{rms} and v'_{rms} intensities, as well as in the turbulence kinetic energy, k (less than 10%). Marked zones in Fig. 6 show the zones with the maximum decrease. Figure 10b) confirms this tendency. However, an increase in the intensity of w'_{rms} (3-4%) was observed (A-square, Fig. 6). All z-planes reflected similar behavior. The flow developed between the fins is similar to that obtained in a plane channel flow. However, the normal component (w'_{rms}), could not entirely develop due to the narrowness of the space between fins. Here, turbulence was created by the wall boundary layers. In Case 4, the space between segments does not allow the full development of these boundary layers. The result was a decrease in the magnitude of the turbulence intensities u'_{rms} and v'_{rms}. Only the component w'_{rms} was favored, by the flow between the interfin zones, as seen in Sec. 6.2. In Fig. 6 the zones with the greatest decrease are within a square.
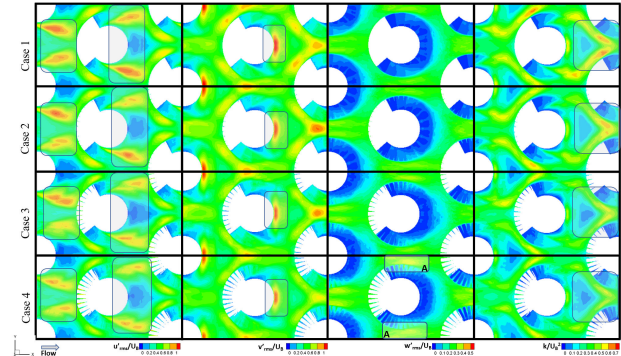

FIGURE 6. Turbulence intensities u'_{rms}, v'_{rms}, and w'_{rms}; and the turbulence kinematic energy, k, in a z-plane, $z/D_0 = 0.11$. Maximum intensities changes are marked (squares).

To understand better the turbulence decreases, see Fig. 7. The wall turbulence feeds on the velocity gradients generated near the wall. When the flow touches the fins and the tubes, the boundary layer develops generating turbulence. If the wall is discontinuous, case 4, the boundary layer development is weak and the turbulence in the flow is lower. Figure 7 shows the u'_{rms} and k contours in the interfin zone and the mean streamwise velocity profiles for three different x-positions. Note the differences in the gradients of the velocity profiles near the wall (profile (1)). Profile (3) does not reach zero-value (wall no-slip condition is not met). These differences generate the decrease in turbulence observed in the contours between cases 1 and 4.

Despite the previous changes observed in the magnitude of the turbulence intensities outside the fin zones, the
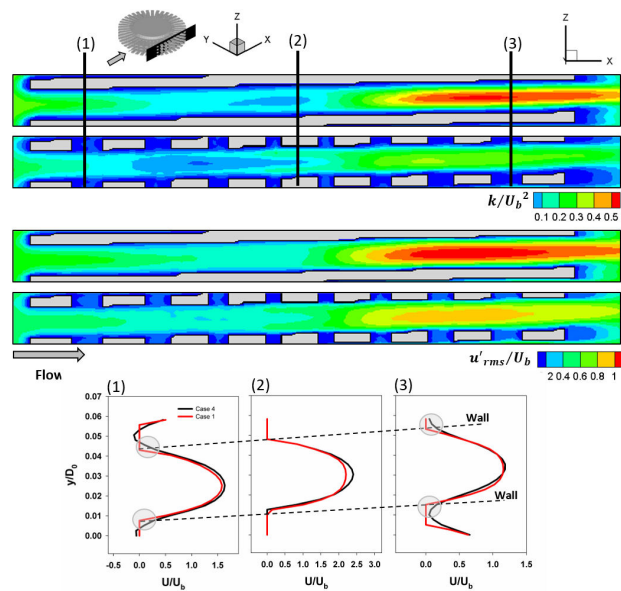

FIGURE 7. Turbulence intensities u'_{rms} and the turbulence kinematic energy, k contours in a y-plane, $y/D_0 = 0.44$. Mean streamwise velocity in three different lines. Circles shoe the profile difference: (1) different slope and (3) Velocity profile does not reach zero value (no-slip condition).
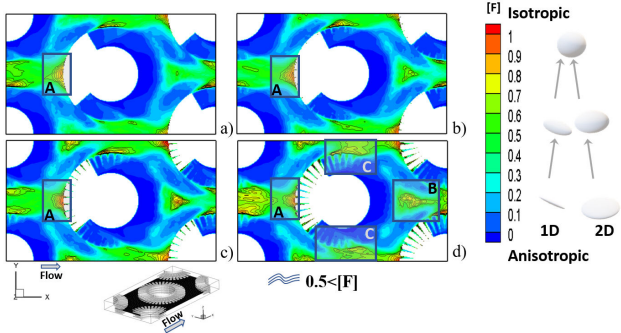
FIGURE 8. The anisotropic state of turbulence parameter $[F]$ contour in a z-plane, $z/D_0 = 0.1$; a) Case 1, b) Case 2, c) Case 3, and d) Case 4. Line contours show $0.5 < [F]$ zones.

anisotropic state of turbulence is also transformed. The turbulence in this flow was highly anisotropic because it has a preferential flow direction (streamwise direction). This flow changed direction around the tubes and transfer turbulence energy from the streamwise (u'_{rms}), to the spanwise component (v'_{rms})(*e.g.*, boundary layers, solid bodies, and wakes).

However, the fins restrict the transfer of turbulence energy to the third direction, w'_{rms}. The impact of the fins on the anisotropic state of turbulence can be seen in Fig. 8. This figure shows the contours of the parameter $[F]$ (Eq. (16)). The fin segmentation promoted the transfer of turbulent energy from the main direction component, u'_{rms}, to the normal component w'_{rms} favoring a less anisotropic state of turbulence. In Figs. 8c) and 8d), the increase in the magnitude of $[F]$ is observed in front (red zone, A-square), behind (B-square), and to the sides of the tubes (C-square). Similar behavior was observed in all z-planes. $[F]$ values closer to 1 indicated a state of turbulence that tended toward isotropy. The line contours in Fig. 8 show the values $0.5 < [F]$. The zones increased from Case 1 to Case 4, corroborating our hypothesis that fin segmentation promotes less anisotropic turbulence.

Figure 9 shows the contours of the three turbulence variables in the y-plane. In this zone, an increase in the component w'_{rms} was observed, mainly in front of the fin segments
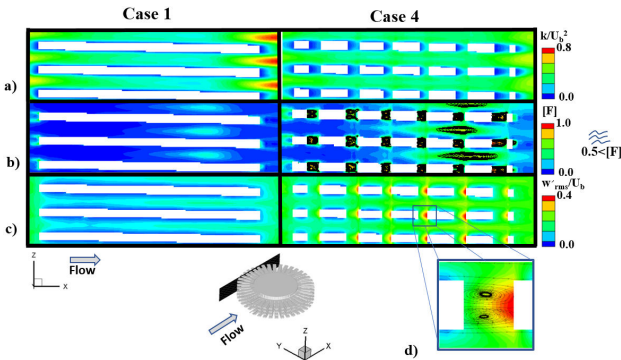

FIGURE 9. Turbulent variables in a y-plane, $y/D_0 = 0.44$, include a) turbulence kinematic energy, k, b) the anisotropic state of turbulence parameter $[F]$, c) turbulence intensity, w'_{rms}, and d) turbulence intensity, w'_{rms}, magnified view of the interfin zone.
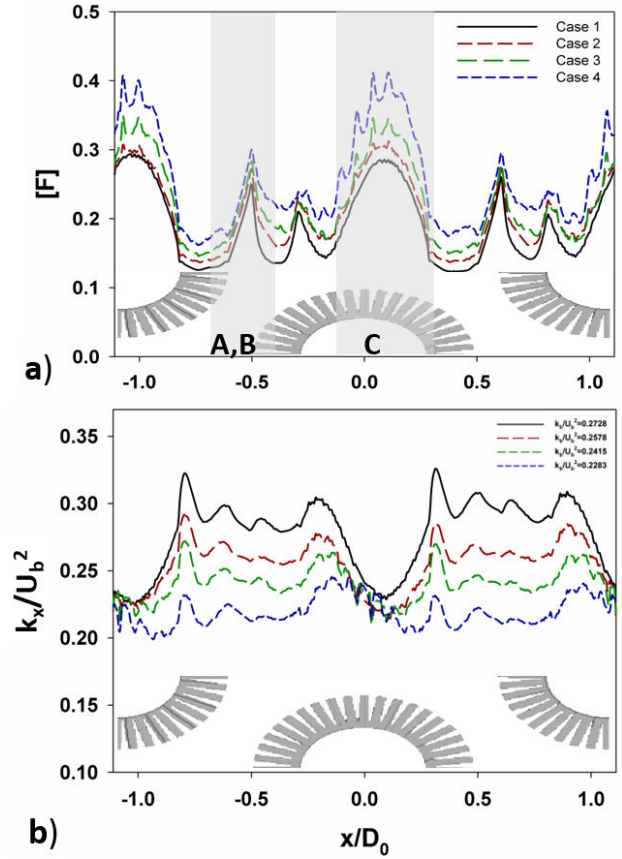

FIGURE 10. Streamwise mean profiles: a) $[F]$ parameter (A-, B-, C-squares in Fig. 8), and b) turbulence kinetic energy, k_x/U_b^2 bulk mean values. In legend: k_b/U_b^2 Eq. (8))).

[Fig. 9c)], where a mean recirculation flow was created [see Fig. d)] (trajectory lines of the mean velocity fields). In Case 4, a slight increase in k was observed (Fig. 9a), but outside the interfin zone, its magnitude was lower than in Case 1. For Case 4, the anisotropic state of the turbulence is closer to isotropy, and contour values of the parameter $[F]$ are near 1 (Fig. 9b). A more isotropic turbulence behavior, where the parameter $[F]$ is closer to unity, could transform the momentum and the energy distribution (work is in progress). Previous works have not reported results on the influence of the anisotropic state of turbulence on heat transfer in similar geometries.

Figure 10 shows the streamwise mean profiles of the $[F]$ parameter and the turbulence kinetic energy k. The values were obtained from a variation of Eq. (8), integrated only in the $y - z$ planes:

$$(\varnothing)_x(t) = \frac{1}{\mathbf{A(y-z)}_{\text{Free\_Total}}} \iint \varnothing(\vec{x},t)\delta_b(\vec{x})dydz, \quad (17)$$

where $\mathbf{A(y-z)}_{\text{Free\_Total}}$ are the free yz-area of every x-plane. The important thing to highlight is the areas where the variables are the maximum. In the case of parameter $[F]$, the maximum value was observed in front of the tubes A-square (Figs. 8 and 10) behind the tubes (B-square) and on the sides

of the tubes, generated mainly by the separation of the boundary layers C-square (Figs. 8 and 10). Figure 10a) shows a third peak at the beginning of the last zone mentioned above. The small peaks in Fig. 10a) (in the C- squares) are the effect of fin segmentation. The streamwise mean maximum values for Case 4 are $[F] \approx 0.4$, and for Case 1, $[F] \approx 0.28$. However, locally, the value can reach close to 0.9 for all cases. See square A in front of the central tube in Fig. 8. For turbulence kinetic energy, the distribution was more uniform. The variable decreased around the tube center. The highest streamwise velocity was observed in this zone (Fig. 4). In this zone, the minimum values of the fluctuations of the principal components are found. However, an increase in the third component, A-square (Fig. 6), was observed for Cases 3 and 4. Figure 10b) shows the bulk mean Eq. (8) values for each case. A maximum decrease of 16% was found between Cases 1 and 4.

7. Conclusions

This study analyzed the effect of fin segmentation depth on turbulence in a helical fin tube bundle. Much of the turbulence generated is due primarily to the boundary layers and the wakes behind the solid bodies. In the case of segmented fins, the discontinuity of fin walls does not allow the complete development of boundary layers, obtaining a reduced turbulence kinetic energy (Fig. 10) of up to 15% in Case 4 compared to Case 1. Despite the decrease in the magnitude of the turbulence, the fin segmentation generated a state of turbulence closer to isotropy, which would transform heat transfer (this work is in progress). This assumption is based on the turbulence transformation observed in the interfin zone, where heat transfer was produced in this flow. Likewise, an intense flow interaction was observed between interfin zones.

1. H. Zhou *et al.*, Research on gas side performance of staggered fin-tube bundles with different serrated fin geometries, *International Journal of Heat and Mass Transfer* **152** (2020) 119509, https://doi.org/10.1016/j.ijheatmasstransfer.2020.119509.

2. E. Naess, Experimental investigation of heattransfer and pressure drop in serrated-fin tube bundles with staggered tube layouts, *Applied Thermal Engineering* **30** (2010)1531, https://doi.org/10.1016/j.applthermaleng.2010.02.019.

3. Y. Ma, *et al*., Experimental investigation of heat transfer and pressure drop in serrated finned tube banks with staggered layouts, Applied Thermal Engineering **37** (2012) 314, https://doi.org/10.1016/j.applthermaleng.2011.11.037.

4. P. Kiatpachai, S. Pikulkajorn, and S. Wongwises, Air-side performance of serrated welded spiral fin-and-tube heat exchangers, International Journal of Heat and Mass Transfer **89** (2015) 724, https://doi.org/10.1016/j.ijheatmasstransfer.2015.04.095.

5. T. Keawkamrop *et al.*, Effect of the segmented fin height on the air-side performance of serrated welded spiral fin and tube heat exchangers, *Case Studies in Thermal Engineering* **35** (2022) 102128, https://doi.org/10.1016/j.csite.2022.102128.

6. E. N. Pis'mennyi, Special features of flow and heat transfer in staggered bundles of transversely finned tubes, *Case Studies in Thermal Engineering* **60** (1991) 676-681, https://doi.org/10.1007/BF00871502.

7. E. Pis'mennyi, Study and application of heat-transfer surfaces assembled from partially finned flat-oval tubes, *Applied Thermal Engineering* **106** (2016) 1075, https://doi.org/10.1016/j.applthermaleng.2016.06.081.

8. F. Papa, Local Velocities and Heat Transfer Coefficients Over Fintubes. Master Thesis, Master's thesis, University of Alabama in Hunstville (1997).

9. Experimental Analysis of Enhanced Heat Transfer and Pressure-Drop of Serrated Finned-Tube Bundles with different Fin Geometries, https://www.researchgate.net/publication/229044286_Experimental_Analysis_of_Enhanced_Heat_Transfer_and_Pressure-Drop_of_Serrated_Finned-Tube_Bundles_with_different_Fin_Geometries.

10. S.R. Mcilwain, A comparison of heat transfer around a single serrated finned tube and a plain finned tube, *International Journal of Research and Reviews in Applied Sciences* **2** (2010), https://www.arpapress.com/Volumes/Vol2Issue2/IJRRAS_2_2_01.pdf.

11. A. Lemouedda *et al.*, Numerical investigations for theoptimization of serrated finned-tube heat exchangers, *Applied Thermal Engineering* **31** (2011) 1393, https://doi.org/10.1016/j.applthermaleng.2010.12.035.

12. B. Anoop, C. Balaji, and K. Velusamy, A characteristic correlation for heat transfer over serrated finned tubes, *Annals of Nuclear Energy* **85** (2015) 1052, https://doi.org/10.1016/j.anucene.2015.07.025.

13. A. Kumar, *et al*., 3D CFD simulations of air cooled condenser-II: Natural draft around a single finned tube kept in a small chimney, *International Journal of Heat and Mass Transfer* **92** (2016) 507, https://doi.org/10.1016/j.ijheatmasstransfer.2015.07.136.

14. R. Hofmann and H. Walter, Experimental and Numerical In-vestigation of the Gas Side Heat Transfer and Pressure Drop of Finned Tubes-Part II: Numerical Analysis, *Journal of Thermal Science and Engineering Applications* **4** (2012) `https://doi.org/10.1115/1.4007125`.

15. E. Martinez *et al.*, Numerical simulation of turbulent air flow on a single isolated finned tube module with periodic boundary conditions, *International Journal of Thermal Sciences* **92** (2015) 58, `https://doi.org/10.1016/j.ijthermalsci.2015.01.024`.

16. A. Kumar *et al.*, 3D CFD simulations of air cooled condenser-III: Thermal-hydraulic characteristics and design optimization under forced convection conditions, *International Journal of Heat and Mass Transfer* **93** (2016)1227, `https://doi.org/10.1016/j.ijheatmasstransfer.2015.10.048`.

17. E. Martinez-Espinosa, W. Vicente, and M. Salinas-Vazquez, Numerical Analysis for Saving Fin Material in Helical Segmented-Tubes, *Applied Thermal Engineering* **110** (2017) 306, `https://doi.org/10.1016/j.applthermaleng.2016.08.061`.

18. E. Martinez-Espinosa **et al.**, Numerical Analysis of Turbulent Flow in a Small Helically Segmented Finned Tube Bank, *Heat Transfer Engineering* **38** (2017) 47, `https://doi.org/10.1080/01457632.2016.1156396`.

19. A. Kumar, J.B. Joshi, and A.K. Nayak, A comparison of thermal-hydraulic performance of various fin patterns using 3D CFD simulations, *International Journal of Heat and Mass Transfer* **109** (2017) 336, `https://doi.org/10.1016/j.ijheatmasstransfer.2017.01.102`.

20. K. Lindqvist and E. Næss, A validated CFD model of plain and serrated fin-tube bundles, *Applied Thermal Engineering* **143** (2018) 72, `https://doi.org/10.1016/j.applthermaleng.2018.07.060`.

21. C. Rajesh Babu *et al.*, CFD analysis of an economizer for heat transfer enhancement using serrated finned tube equipped with variable fin segments, *Materials Today: Proceedings* **45** (2021) 222, `https://doi.org/10.1016/j.matpr.2020.10.422`.

22. M. Salinas-Vázquez *et al.*, Large eddy simulation of fully-developed flow in a helical segmented-fin tube bundle, *Applied Mathematical Modelling* **98** (2021) 595, `https://doi.org/10.1016/j.apm.2021.05.027`.

23. M. S. Vázquez and O. Métalis, Large-eddy simulation of the turbulent flow through a heated square duct, *Journal of Fluid Mechanics* **453** (2002) 201-238, `https://doi.org/10.1017/S0022112001006887`.

24. D. Gottlieb and E. Turkel, Dissipative Two-Four Methods for Time-Dependent Problems, Mathematics of Computation **30** (1976) 703, `https://www.jstor.org/stable/2005392`.

25. O. Simonin and M. Barcouda, Flow through staggered tube bundle Case 78, ERCOFTAC classic database (2007), `https://cfd.mace.manchester.ac.uk/cgi-bin/cfddb/prpage.cgi?78&EXP&database/cases/case78/Case_data&database/cases/case78&cas78_head.html&cas78_desc.html&cas78_meth.html&cas78_data.html&cas78_refs.html&cas78_rsol.html&1&0&0&0&1&unknown`.

26. T. Poinsot and S. Lelef, Boundary conditions for direct simulations of compressible viscous flows, *Journal of Computational Physics* **101** (1992) 104, `https://doi.org/10.1016/0021-9991(92)90046-2`.

27. M. Lesieurand O. Metais, New Trend sin Large-Eddy Simulations of Turbulence, *Annual Review of Fluid Mechanics* **28** (1996) 45, `https://doi.org/10.1146/annurev.fl.28.010196.000401`.

28. M. Lesieurand P. Compte, Large-eddy simulation of compressible turbulent flows. Turbulence in Compressible Flows, AGARD Rep 819, AGARD/VKICourse (1997), `https://www.sto.nato.int/publications/AGARD`.

29. E. David, Modélisation des écoulements compressibles et hypersoniques: une approche instationnaire, Ph. D. thesis, Grenoble INPG (1993).

30. E. Olssonand G. Kreiss, A conservative level set method for two phase flow, *Journal of Computational Physics* **210** (2005) 225, `https://doi.org/10.1016/j.jcp.2005.04.007`.

31. E. Olsson, G. Kreiss, and S. Zahedi, A conservative level set method for two phase flow II, *Journal of Computational Physics* **225** (2007) 785, `https://doi.org/10.1016/j.jcp.2006.12.027`.

32. M. Salinas-Vázquez *et al.*, Large Eddy Simulation of a flow through circular tube bundle, Applied Mathematical Modelling **35** (2011) 4393, `https://doi.org/10.1016/j.apm.2011.03.003`.

33. R. P. Fedkiw *et al.*, A Non-oscillatory Eulerian Approach to Interfaces in Multimaterial Flows (the Ghost Fluid Method), *Journal of Computational Physics* **152** (1999) 457, `https://doi.org/10.1006/jcph.1999.6236`.

34. G.-S. Jiangand P. Damping, Weighted ENO Schemes for Hamilton-Jacobi Equations, *J. Sci. Comp.* **21** (2000) 2126, `https://doi.org/10.1137/S106482759732455X`.

35. R. Magos-Alba, Numerical simulation of the flow around a tube bundle with helical segmented fins. (Simulación numérica de flujos alrededor de un banco de tubos de aleta helicoidal segmentada), Master's degree thesis, Universidad Nacional Autónoma de México, México (in Spanish). (2019), Avaliable in `https://tesiunam.dgb.unam.mx`.

36. Visualizing turbulence anisotropy in the spatial domain with componentality contours (Center for Turbulence Research, *Annual Research Briefs.* (2014), `https://api.semanticscholar.org/CorpusID:29497825.`.

37. N. Hamilton, M. Tutkun, and R.B. Cal, Anisotropic character of low-order turbulent flow descriptions through the proper orthogonal decomposition, *Phys. Rev. Fluids* **2** (2017) 014601, `https://doi.org/10.1103/PhysRevFluids.2.014601`.

38. J. L. Lumley and G.R. Newman, The return to isotropy of homogeneous turbulence, *Journal of Fluid Mechanics* **82** (1977) 161-178, `https://doi.org/10.1017/S0022112077000585`.

39. E. M.-E.L. CLara-Guzman, M. Salinas-Vazquez and W. Vicente, Numerical Study of the effect of potato cuboids separation in a convecting drying, *Drying Technology.* (2023), `https://doi.org/10.1080/07373937.2022.2157009`.